ACS ES&T Engineering

pubs.acs.org/estengg

Article

Joule Heating Induced Reductive Iron−Magnesium Bimetallic Nanocomposite for Eminent Heavy Metal Removal

Published as part of ACS ES&T Engineering virtual special issue "Free Radical Chemistry in Environmental Engineering Systems".

Chao Jia, Liming Sun, Xuan Wu, Fengbo Yu, Litao Lin, Zhelin He, Jie Gao, Shicheng Zhang,* and Xiangdong Zhu*

Cite This: https://doi.org/10.1021/acsestengg.3c00514

Read Online

ACCESS | Metrics & More | Article Recommendations | Supporting Information

ABSTRACT: Fe^0-based materials exhibit great power in removing heavy metals, but their passivation issues remain a challenge. Guided by the synergistic effects within bimetallic modifications, a novel reductive FeMg bimetallic nanocomposite (FeMg/NC) was constructed using flash Joule heating technology. The ultrafast heating and quenching process achieved a phase-fusional structure comprising Fe^0 and Mg^0 encapsulated in the resulting aromatic-carbon layer. Incorporation of highly reductive Mg^0 into Fe^0-based material led to an approximately 2−3 times enhancement in pollutant removal efficiency compared to monometallic nanocomposites. Experiments and theoretical calculations revealed that this augmented removal efficiency arose from the FeMg dual-site synergistic effect, facilitating the interaction between FeMg/NC and the targeted pollutants. That is, adsorption led to the directional inward diffusion of pollutants, and the outward release of electrons from this formed phase-fusion structure was accelerated via the electron delocalization effect. Therefore, FeMg/NC exhibited excellent removal capacities for typical heavy metals (including Cr(VI), Sb(V), Ni(II), and Cu(II)). This study demonstrates the flexibility of Joule heating technology for constructing bimetallic nanocomposite, which can effectively address heavy metal pollution and opens up endless possibilities for developing more impactful environmental remediation materials.

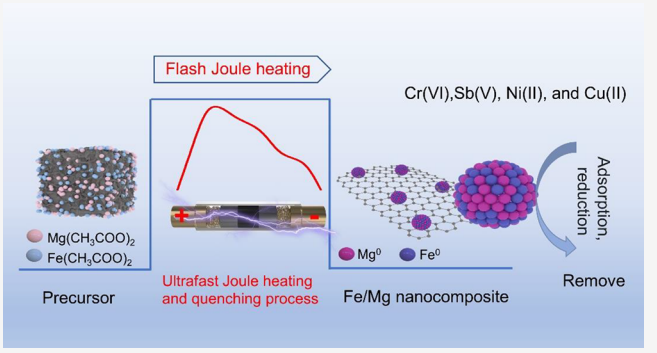

KEYWORDS: *zero-valent iron, bimetallic modification, flash Joule heating, heavy metals removal*

INTRODUCTION

The unregulated discharge of heavy metal-containing wastewater (such as Cr(VI), Sb(V), Ni(II), and Cu(II)) from mining, printing and dyeing, and other human activities, poses a severe threat to the self-operation of the ecosystem.[1,2] Fe^0-based materials are recognized as excellent electron donors and reductants for environmental remediation due to their strong reactivity.[3−5] Notwithstanding these merits, their efficiency in heavy metal removal remains unsatisfactory due to passivation and aggregation issues encountered in practical applications.[6,7] To address this limitation, an effective strategy involves incorporating a secondary metal to form Fe-based bimetallic nanoparticles, thereby enhancing their pollutant removal activity via the formed galvanic effect or hydrogen atom generation.[8−10] However, most metals with positive redox potential or catalytic properties, such as Pd, Pt, Ag, Cu, Ni, and Pb, are often limited by cost or toxicity.[11−13] Therefore, it is imperative to select cost-effective and environmentally friendly metals for bimetallic modification.

As an abundant element on earth, eco-friendly magnesium (Mg) easily achieves the above goals.[14] Moreover, Mg^0 (E^0 = −2.36 V) exhibits a lower standard electrode potential than Fe^0 (E^0 = −0.44 V) in theory, rendering it more favorable for the reduction of refractory contaminants.[15,16] However, conventional methods for preparing Fe^0-based materials, such as carbothermal reduction, H_2 reduction, and $NaBH_4$ reduction methods, have a negligible impact on the development of Mg activity.[17] These methods typically result in aggregated high-valent Mg (such as MgO), weakening its strong chemical reducibility and leading to a low efficiency in applications.

Recently, carbon-assisted flash Joule heating (FJH), a facile and scalable technology, has demonstrated great potential for

Received: October 27, 2023
Revised: January 11, 2024
Accepted: January 11, 2024

rapidly synthesizing reductive Fe/carbon nanocomposites with a unique millisecond heating and quenching process.[18,19] In this paper, we aim to introduce and enhance Mg activity with the assistance of FJH technology to fabricate highly reductive FeMg bimetallic nanocomposites (FeMg/NC) on a carbon matrix. First, it can be predicted that the crack of chemical bond in the Fe/Mg-containing precursors will form high chemical activity components (such as Fe^0 and Mg^0) in the rapid heating process (~50 ms, >3000 K) and then subsequently undergo a phase-solid-melt reaction to form the bimetallic structure.[20] This phase-fusional structure is expected to reinforce atomic orbital hybridization, improving the reductive capacity via electron delocalization.[7,21] Additionally, the rapid quenching process is likely to hinder the aggregation of these components, facilitating the production of highly reactive metal particles with minor sizes.[22] Moreover, the ultrahigh temperature and electric shock action can convert the carbon matrix into graphene to sustain both the high stability and activity of these reductive components.[18,23] However, it is imperative to verify whether the obtained material can enhance the pollutant removal ability. In this regard, the mechanism of the pollutant removal enhancement must be clarified.

Accordingly, FeMg/NC was synthesized using FJH technology to (1) examine the effect of bimetallic modification on the removal ability of typical heavy metal-containing wastewater (including Cr(VI), Sb(V), Ni(II), and Cu(II)); (2) investigate the interactions between their structural evolution and corresponding heavy metal removal performance; and (3) explore the mechanism involved in bimetallic modification for removing these pollutants. Finally, as a proof of concept, simulated heavy metal-containing wastewater was employed to showcase the great potential of FeMg/NC for practical applications.

MATERIALS AND METHODS

FJH-Induced Synthesis of FeMg Bimetallic Nanocomposite. Details of the used chemicals and materials were provided in Text S1 (Supporting Information). For the sustainable production of reductive materials, 0.1 g of prepared raw material was put into a quartz tube and compressed with copper electrodes to reduce the raw material resistance (Text S2 and Table S1). Then, this raw material was subjected to FJH in a vacuum desiccator (~0.6 psi) to avoid sample oxidation and operated twice consecutively at the desired discharge voltage (250 V). In the typical process, the raw materials were driven by the generated current to emit dazzling visible light and showed a uniform temperature distribution in the quartz tube (Figures S1−S4). This flash reaction lasted less than 50 ms from the start to the end, realizing the key two steps involving rapid heating to about 2940 K and quenching to room temperature. After the FJH reaction, the obtained samples were collected and named as X/NC (including Fe/NC, Mg/NC, and FeMg/NC), and X represents the different types of metal salts. Notably, the sample derived directly from the parent hydrochar after FJH treatment was denoted as shockchar.

Characterizations of Materials. The morphologies and elemental distributions of these samples were recorded by using a high-resolution transmission electron microscope (HR-TEM, Tecnai G2 F20 S-Twin, FEI, USA) equipped with energy dispersive X-ray spectrometry (EDX) and high-angle annular dark-field (HAADF) images. The ingredients and crystalline phase of samples were performed by X-ray diffraction (XRD, Ultima IV, Rigaku, Japan) with Cu Kα radiation at 40 kV and 40 mA in the 2θ range of 10−90°. The element species of samples were measured by X-ray photoelectron spectroscopy (XPS, ESCALAB 250 XI, Thermo, USA) at a base pressure of 10^{-8} to 10^{-10} mbar. The binding energies of high-resolution spectra were calibrated at a C 1s of 284.6 eV. The graphitization degree of samples was carried out using an XploRA Raman spectrometer with a 532 nm (5 mW) laser source. The surface area and porosity of samples were acquired by N_2 adsorption/desorption at 77 K using a Quantachrome Autosorb iQ2 instrument. Electrochemical tests (Tafel scans and Electrochemical Impedance Spectroscopy (EIS) curves) of these samples were recorded by using an electrochemical workstation (CHI-600E, Chenhua, China, Text S3). The test methods of the voltage, current, and temperature profile in the FJH process have been reported in our previous work.[24] Other characterizations used to simulate the temperature distribution in the FJH process were also detailed in Text S4 and Table S2.

Batch Experiments. To explore the versatility of the FeMg/NC sample, several representative heavy metals (including Cr(VI), Sb(V), Ni(II), and Cu(II)) were adopted in the batch experiments. The Cr(VI) removal experiments were first performed in an oxygen-free aqueous solution at room temperature. The initial pH value of the Cr(VI) solution was adjusted to 4.0. Typically, the reactants (1 g/L) were added into a serum bottle with 40 mL of Cr(VI) solutions (20 mg/L). Then, the supernatant was collected by filtration using a 0.22 μm nylon syringe filter at certain intervals for analysis of the Cr(VI) concentration. After the reaction, the reactants were also collected for further characterization. Notably, the batch removal experiments of other heavy metals (including Sb(V), Ni(II), and Cu(II)) were similar to those of the Cr(VI) solution. The only difference was that the reactants (1 g/L) were added to a serum bottle containing 10 mg/L Sb(V), 10 mg/L Ni(II), and 20 mg/L Cu(II) solutions, respectively.

In addition, taking the removal of Cr(VI) as an example, the effect of environmental factors on the pollutant removal efficiency by the FeMg/NC sample was investigated. Batch removal experiments of Cr(VI) were conducted with different pH values (3−11), doses (0.5−2 g/L), and solution atmospheres (Ar and air). The pH value of the solution was adjusted with NaOH and HCl. These experiments were performed in triplicate, and the averaged results were presented.

Further, the potential of the FeMg/NC sample was explored through the removal experiment of simulated heavy metal-containing wastewater. In this paper, the simulated wastewater can be traced to some published literature.[25,26] Briefly, the initial Cr(VI), Sb(V), Ni(II), and Cu(II) concentrations of simulated wastewater were set to 5 mg/L, with 10 mg/L humic acid as the natural organic matter (NOM), and 1 mmol/L $NaHCO_3$, 1 mmol/L Na_2SO_4, 5 mmol/L NaCl, and 0.8 mmol/L $CaCl_2$ as the background electrolytes.

Analytical Methods. The concentration of Cr(VI) was measured with the 1,5-diphenylcarbazide colorimetric method.[7] Total dissolved Fe and dissolved Fe(II) concentrations were quantified using the 1,10-phenanthroline colorimetric method.[21] The Cr, Mg, Ni, Cu, and Fe concentrations were measured by inductively coupled plasma mass spectrometry (ICP-OES, PerkinElmer Optima-8000). The Sb concentration was measured using a hydride generation-atomic fluorescence spectrometer system (HG-AFS) coupled with an AFS-8520

https://doi.org/10.1021/acsestengg.3c00514
ACS EST Engg. XXXX, XXX, XXX−XXX

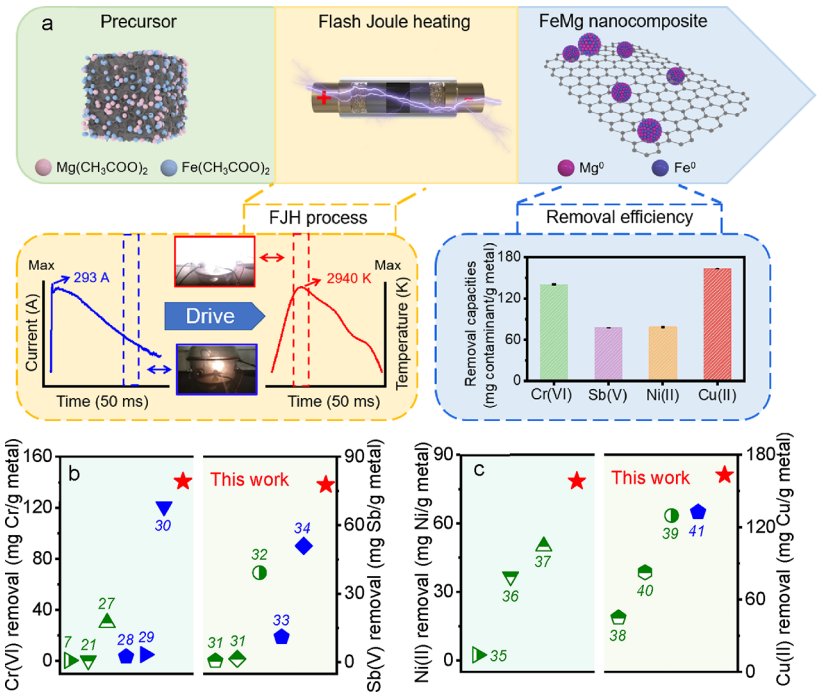

Figure 1. Synthesis and heavy metal removal capacities of FeMg bimetallic nanocomposites (FeMg/NC). (a) Schematic diagram for the mechanism of synthesizing FeMg/NC by carbon-assisted flash Joule heating (FJH) technology (involving the FJH process and removal efficiency of various heavy metals by FeMg/NC sample). Comparison of (b) Cr(VI) and Sb(V), and (c) Ni(II) and Cu(II) removal capacities for the FeMg/NC sample and previously reported ones (The semisolid shape marked with green represent the modified ZVI samples and the solid shape marked in blue represent the bimetallic samples. The detailed information on these materials was shown in Tables S3−S6).

spectrometer (Beijing Haiguang Instrument CO., China). Details for density functional theory (DFT) theoretical calculation were further provided in Text S5.

RESULTS AND DISCUSSION

Influence of Bimetallic Modification on the Removal of Heavy Metals. As illustrated in Figure 1a, the instantaneous ultrahigh temperature triggered by the FJH reaction was successfully used to fabricate the FeMg/NC sample with a phase-fusional structure. The feasibility of the as-prepared FeMg/NC sample was first evaluated for removal of typical heavy metal pollutants, including Cr(VI), Sb(V), Ni(II), and Cu(II). Compared with the Mg/NC and Fe/NC samples, the highly reductive FeMg/NC sample exhibited an excellent removal efficiency for these pollutants (inset: Figure 1a and Figures S5−S8), which may be attributed to the intrinsic structural differences caused by the bimetallic modification. Impressively, these pollutant removal capacities of the FeMg/NC sample reached 141 mg Cr/g metal, 77.7 mg Sb/g metal, 78.5 mg Ni/g metal, and 163.3 mg Cu/g metal, which were higher than those of reported materials (Figure 1b,c and Tables S3−S6).[7,21,27−41] This may be ascribed to the effective enhancement of Mg activity by FJH technology, resulting in a phase-fusional structure that can effectively interact with the target pollutants.[19] Notably, the reduction of these heavy metals were accompanied by many competitive reactions, such as oxygen reduction, hydrogen evolution, and reactions with other coexisted impurities.[42] Although the standard electrode potential of Mg^0 is lower than that of Fe^0, the reductive removal of Cr(VI) by Fe/NC was higher than that of Mg/NC (Figure S5).

As shown in Figures S5 and S8, the pollutant removal curves conformed to pseudo-first-order reaction kinetic equations, indicating that these reactions were mainly chemisorption. Bimetallic modification improved the removal rate of these pollutants to more than 2 times that of the unmodified materials. Considering that BET surface area might influence the heavy metal removal performance,[7] we calculated the BET surface area normalized heavy metal removal rate constant k' (Text S6). As shown in Figure S9, the k' value of the FeMg/NC sample was also higher than that of Fe/NC and Mg/NC samples, excluding the contribution of BET surface area enhancement to the removal performance of these heavy metals. In addition, the adsorption effect of shockchar sample for these pollutants was only 5−10%, indicating that it only provides adsorption sites in pollutants removal (Figure S10).[19]

The versatility of the FeMg/NC sample is also a key indicator for wastewater treatment. Benefiting from the oxygen resistance of the carbon layer, there was no prominent difference in the removal efficiency of Cr(VI) under anaerobic and aerobic conditions (Figure S11a).[19] Figure S11b shows the removal rate of Cr(VI) at the reaction equilibrium under different initial pH conditions. Although a similar pH-dependent reactivity was observed for the FeMg/NC sample, it still exhibited an excellent Cr(VI) removal ability within 60 min at different pH values, indicating that the FeMg/NC sample could significantly promote Cr(VI) removal over a wide pH range. In addition, the number of adsorption and reduction sites is usually related to the dosage of material.[12] As shown in Figure S12, when the dosage of the FeMg/NC sample was increased to 2 g/L, the removal efficiency of Cr(VI) was significantly increased to 97.6%. In summary, it can be inferred that the structural changes caused by bimetallic modification may be the main reason for the improved removal ability of the FeMg/NC sample for typical heavy metals.

https://doi.org/10.1021/acsestengg.3c00514
ACS EST Engg. XXXX, XXX, XXX−XXX

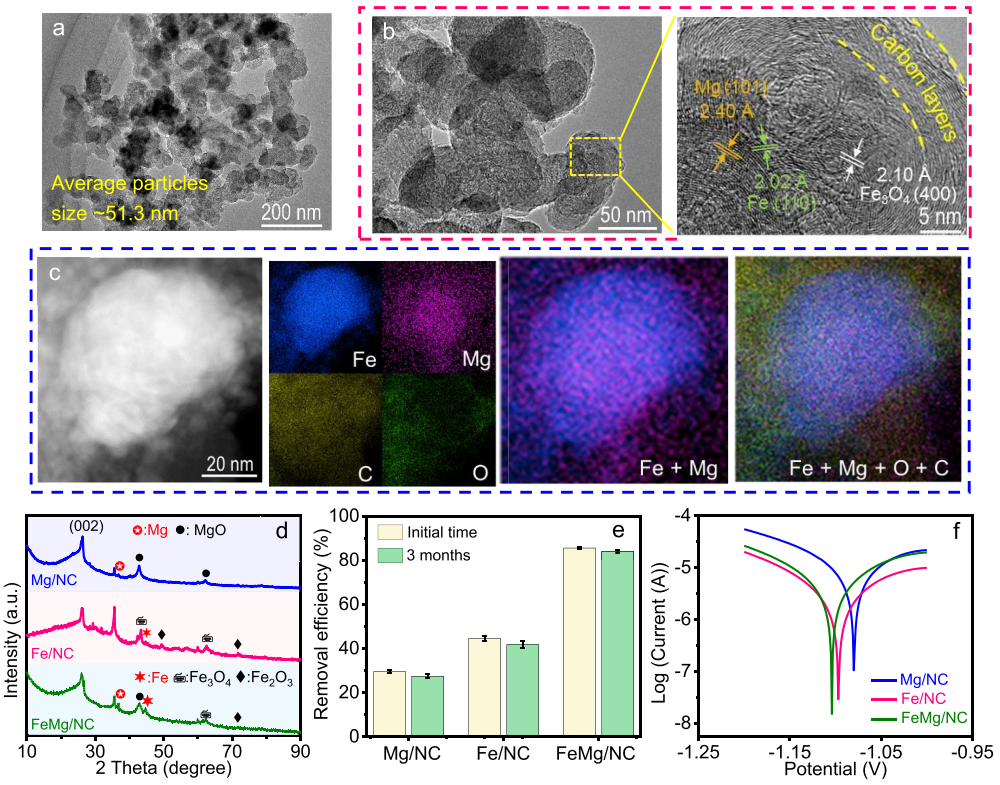

Figure 2. Electro-microscopy and surface chemical property analysis. (a) TEM images of FeMg/NC. (b) High-resolution transmission electron microscopy (HR-TEM) images of FeMg/NC sample. (c) High-angle annular dark-field (HAADF) images of FeMg/NC sample and the corresponding elemental mapping of Mg, Fe, O, C, and their overlapped image. (d) XRD patterns of Mg/NC, Fe/NC, and FeMg/NC samples, respectively. (e) Stability analysis of various samples during Cr(VI) removal (note: all the samples are exposed to the air for 3 months). (f) Tafel curves of Mg/NC, Fe/NC, and FeMg/NC samples, respectively.

Effect of Bimetallic Modification on the Evolution of Reductive Structure. To understand the impact of the bimetallic modification on the removal of these heavy metals, the structural evolution of the FeMg/NC sample during the FJH process was further analyzed. As presented in Figure 2a,b and Figure S13, the morphology of the FeMg/NC sample was similar to those of the Fe/NC and Mg/NC samples. It mainly maintained a quasi-spherical shape, indicating the flexibility of the Fe and Mg architecture evolution during the FJH reaction. However, the incorporation of Mg and Fe into the Fe−Mg framework increased the slight changes in its diameter or length (Figure S14), which may be caused by the nucleation and growth of the interactions between these metal elements during the FJH process.[43] Furthermore, the element mapping image in Figure 2c reveals a highly uniform distribution of Fe and Mg, confirming the homogeneous dispersion of both the Fe and Mg metal centers within the same framework of the FeMg/NC topology rather than a simple mixture. This unique ultrafast heating/quenching function of the FJH reaction facilitates the fusion between Fe and Mg, which is beneficial for enhancing the atomic orbital hybridization ability and improving the reduction ability via the electron delocalization effect.[44,45]

In the HAADF image, certain bright cores were observed in various samples without significant color differences, corresponding to Fe^0 or Mg^0 (Figure 2c and Figure S15). In addition, the atomic-scale TEM image and the corresponding fast Fourier transform (FFT) pattern exhibited perfect crystallinity with lattice spacing (0.24 and 0.22 nm), matching well with the Mg (101) and Fe (110) facet, which was consistent with the XRD patterns (Figure 2b,d and Figure S16). Furthermore, the XPS spectra indicated an abundance of Mg and Fe species, primarily involving Fe^0, Mg^0, and their oxides (Figure S17 and Table S7). These reductive components, resulting from the breaking of chemical bonds of the Fe- and Mg-containing precursors in the rapid heating process, exhibited an indelible role in the removal of the aforementioned heavy metals. Notably, certain metal oxides are also inevitably produced simultaneously during the thermal decomposition of these metal precursors, which is conducive to the adsorption of pollutants.[12]

In addition, the HAADF images clearly indicated an absence of a dense oxide shell in these metal nanoparticles, which was consistent with the scattering distribution of the O and the mapping of overlapping elements contained in O, Fe, or Mg (Figure 2c and Figure S15). This unique structure that broke the insulation of the oxide layer was conducive to improving the electron transfer efficiency between the FeMg/NC sample and pollutants. Importantly, the aromatic-carbon layer formed by the parent carbon-based support during the FJH process (Figure S18 and Table S8) can maintain the stability and activity of these reductive components internally and complete the external adsorption of target pollutants.[19] As confirmed by the HR-TEM images (Figure 2b and Figure S16), the metal nanoparticles were tightly encapsulated by the formed aromatic-carbon layer. Therefore, the Mg/NC, Fe/NC, and FeMg/NC samples exhibited outstanding stability, as validated by their high Cr(VI) removal reactivity even after exposure to air for three months (Figure 2e). Generally, these surface stabilizers hinder the electron transfer of the Fe core to the

https://doi.org/10.1021/acsestengg.3c00514
ACS EST Engg. XXXX, XXX, XXX−XXX

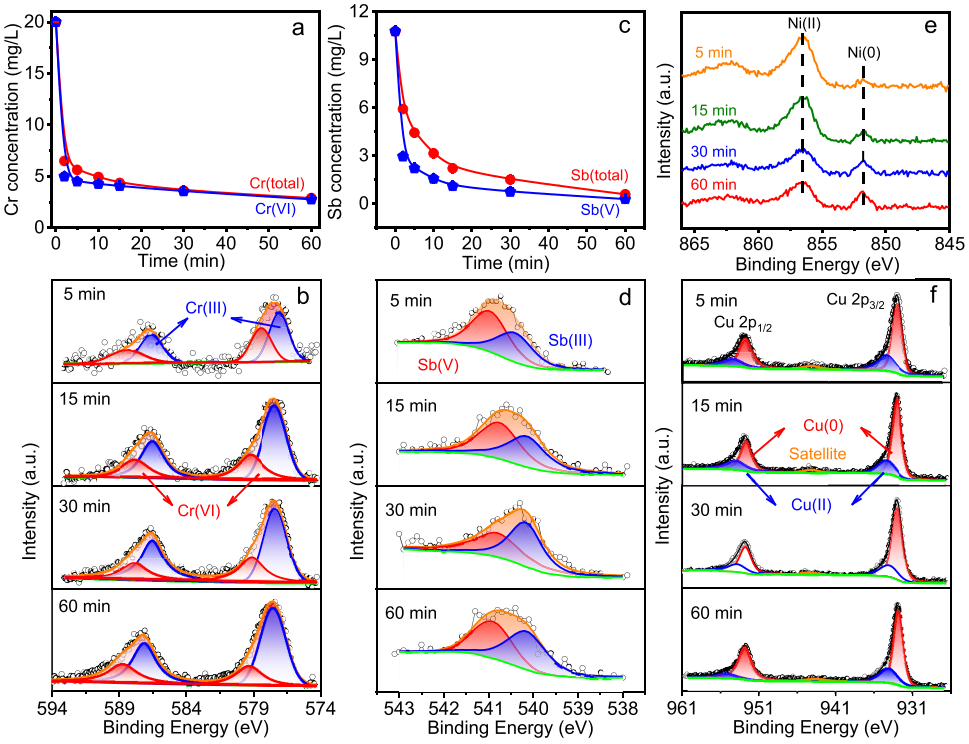

Figure 3. Removal performance and reductive evolution of FeMg/NC during heavy metals removal process. (a) Total Cr and Cr(VI) removal curves of FeMg/NC sample. (b) Time evolution of Cr 2p XPS spectrum during the Cr(VI) removal with FeMg/NC sample. (c) Total Sb and Sb(V) removal curves of FeMg/NC. (d) Time evolution of Sb 3d XPS spectrum during the Sb(V) removal with FeMg/NC sample. (e) Time evolution of Ni 2p XPS spectrum during the Ni(II) removal with FeMg/NC sample. (f) Time evolution of Cu 2p XPS spectrum during the Cu(II) removal with FeMg/NC sample.

pollutant.[46] However, the FeMg/NC sample presented a faster corrosion rate, as this sample exhibited a higher negative free corrosion potential (−1.104 V) than Fe/NC and Mg/NC samples (−1.080 and −1.097 V) in an aqueous environment (Figure 2f).[7] As shown in Figure S19, the lower resistance behavior induced by bimetallic modification also accelerated the electron transfer, resulting in excellent heavy metal removal performance of the FeMg/NC sample.[42,47] In conclusion, the flexibility of the Fe and Mg architecture evolution was endowed by FJH technology to form a highly reductive phase-fusional structure, which is key to improving the heavy metal removal ability of FeMg/NC sample.

Inspired by the aforementioned results and discussion, we evaluated the impact of the internal structural evolution of the FeMg/NC samples on their reduction performance by precisely regulating the FJH parameters and the metal loading ratio. Multiple discharge voltages, ranging from 150 to 250 V, were first adopted to assess the Cr(VI) removal of the obtained FeMg/NC samples. As illustrated in Figure S20, the FeMg/NC sample prepared at a high-voltage (250 V) exhibited excellent reduction efficiency. This is because increasing the discharge voltage increases the input power of the system, resulting in a higher reaction temperature and inducing a more intense FJH reaction (Figures S21 and S22). This high temperature can more easily promote the fusion of Fe and Mg in the FeMg/NC sample, increasing their active sites within a unit of the BET surface area, as confirmed by XPS analysis, the BET surface area, and Tafel curves (Figures S23−25 and Table S9). In addition, the redox potential of Mg is lower than that of Fe, which may improve the reduction capability of the FeMg/NC sample to a certain extent.[15] The subsequent Tafel results can support this inference (Figure S26). As depicted in Figure S27, the larger BET surface area was corresponding to the more incorporated active, which was conducive to promoting sufficient exposure of the active sites (Figure S28 and Table S10).[2] Ultimately, the removal efficiency and rate constant k' of Cr(VI) can be effectively improved by regulating the ratio of Fe and Mg in the FeMg/NC samples (Figure S29).

Reduction Adaptability of Fe/Mg Bimetallic Nanocomposite in Heavy Metal Removal. As expected, the concentration trend of total Cr was consistent with that of Cr(VI) during the removal process, indicating that Cr was removed from the solution (Figure 3a). The rapidly changing pH values were strongly consistent with the Cr(VI) removal process of these samples, suggesting an intense reductive process that consumes protons (Figure S30).[7] The Cr 2p XPS spectra position on the surface of the reacted FeMg/NC sample was well fitted by the Cr(III) and Cr(VI) species (Figure 3b). The peaks at 576.6 and 586.6 eV were attributed to Cr(III) species, while the peaks at 577.7 and 588.5 eV belonged to Cr(VI) species. An obvious Cr(III) species could be observed at the reaction time from 5 to 60 min, indicating that most of the adsorbed Cr(VI) was reduced to Cr(III) by the FeMg/NC sample and subsequently fixed on its surface (Table S11).

Simultaneously, the Sb(V), Ni(II), and Cu(II) removal processes of the FeMg/NC samples were also monitored. As shown in Figure 3c, the concentration trend of the total Sb was consistent with that of Sb(V) during the removal process, suggesting that Sb(V) was reduced and subsequently removed. The removal of Ni and Cu by the FeMg/NC sample is presented in Figures S7a and 8a. Furthermore, the valence

https://doi.org/10.1021/acsestengg.3c00514
ACS EST Engg. XXXX, XXX, XXX−XXX

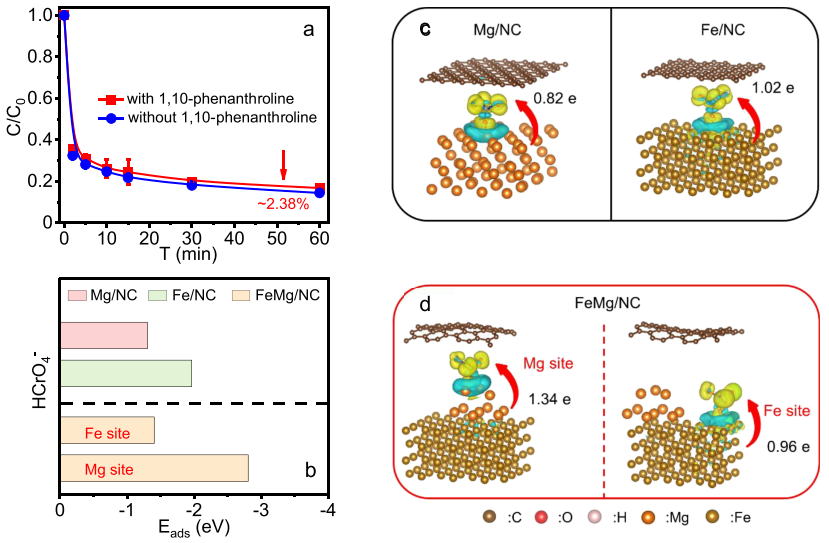

Figure 4. Reaction mechanism analysis. (a) Cr(VI) removal curves of FeMg/NC sample in the absence of 1,10-phenanthroline or the presence of 1,10-phenanthroline. (b) Adsorption energies (E_{ads}) of $HCrO_4^-$ coordinated with Mg/NC, Fe/NC, and FeMg/NC samples, according to density functional theory (DFT) calculations. DFT calculation of the charge-density difference in $HCrO_4^-$ adsorbed on (c) Mg/NC and Fe/NC, and (d) FeMg/NC (including Fe site and Mg site) samples, respectively. The yellow and blue isosurfaces represent the charge accumulation and depletion region.

state changes of these metals in the FeMg/NC sample were analyzed using XPS spectroscopy. In Figure 3d, the XPS spectra of the Sb peak positions on the surface of the reacted FeMg/NC sample were also fitted as Sb(III) and Sb(V) species, respectively.[31] The reduced state of Sb(III) was the major species, accounting for approximately 56.0% (Table S12). Similarly, the Ni 2p XPS spectra on the surface of the reacted FeMg/NC sample deconvoluted into two typical peaks at 856.6 and 851.8 eV, respectively, attributed to adsorbed Ni(II) and reduced Ni(0) (Figure 3e).[27] After only 5 min of reaction, Ni(0) (6.36%) was observed, indicating that adsorbed Ni(II) was rapidly reduced to Ni(0) by the FeMg/NC sample (Table S13). Coincidentally, the characteristic peaks of Cu(0) appeared at 932.9 and 952.7 eV in the Cu $2p_{3/2}$ and Cu $2p_{1/2}$ regions, respectively (Figure 3f). The satellites combined with the relatively weak peak at 944.4 eV validated the presence of CuO or $Cu(OH)_2$.[38] These results demonstrated that most of the uncompleted Cu(II) was removed by the FeMg/NC sample in the reduced form of Cu(0) (72.6%), while other Cu(II) was immobilized by surface precipitation and adsorption onto the corrosion products (Table S14).

Insight into Mechanism of Enhanced Removal by Bimetallic Modification. As exemplified by the Cr(VI) removal, the mechanism of bimetallic modification for enhancing the removal performance was elucidated. Considering Fe(II), it is inherent to the FeMg/NC sample or generated by iron core corrosion, which is an essential active species in the process of reducing heavy metals. As shown in Figure S31a,b, the amount of Fe(II) released in the Cr(VI)- or Cr(VI)-free solution indicates that it may participate during the reduction of Cr(VI). However, the Cr(VI) removal process of the FeMg/NC and Fe/NC samples was not inhibited by the addition of 1,10-phenanthroline (Figure 4a and Figure S32), indicating that Fe(II) was not the main reactive substance in the FeMg/NC sample to remove Cr(VI). Therefore, it can be inferred that the reductive components (Fe^0 or Mg^0) in the FeMg/NC sample are the main reason for the enhanced reduction of Cr(VI) (eqs 1 and 2), which can be confirmed in Figure S31c,d.

$$3Fe^0 + 2HCrO_4^- + 14H^+ \rightarrow 3Fe^{2+} + 2Cr^{3+} + 8H_2O \quad (1)$$

$$3Mg^0 + 2HCrO_4^- + 14H^+ \rightarrow 3Mg^{2+} + 2Cr^{3+} + 8H_2O \quad (2)$$

Further, to reveal the role of the synergistic effect in enhancing the reduction performance, theoretical calculations were performed using two basic model structures, namely, single metal and bimetallic structure systems. For the FeMg/NC sample, the Fe active species was used as the benchmark model and a portion of the Mg active species was constructed on this basis. While the Mg/NC and Fe/NC samples were constructed by taking the corresponding active species as the benchmark model (Figure S33). In addition, Cr(VI) was adsorbed onto the inner active sites after crossing the thin aromatic-carbon layer to complete the construction of the entire theoretical model (Figure S34). The DFT results indicated that the adsorption energy of Cr(VI) at the Mg site (−2.81 eV) or Fe site (−1.41 eV) on FeMg/NC was lower than that on Mg/NC (−1.97 eV) and Fe/NC (−1.30 eV) (Figure 4b,c), which may contribute to the enhanced Cr(VI) removal performance. Charge-density difference calculations revealed that Cr(VI) adsorbed on the Mg/NC or Fe/NC samples accepted electrons from Mg^0 or Fe^0 via a single-channel pathway. In contrast, Cr(VI) adsorbed on the FeMg/NC sample captured electrons in diverse manners, as two types of active sites can combine with Cr(VI). The difference in the electron transfer pathway led to a better electron-withdrawing ability of Cr(VI) on the bimetallic structure surface, as reflected by its higher electron transport quantity (Figure 4c), which was beneficial for the subsequent reduction of Cr(VI).

In this paper, the theoretical and experimental results demonstrated that this bimetallic structure favors the adsorption of these heavy metals on its surface-active sites with a much lower adsorption energy and the electron

https://doi.org/10.1021/acsestengg.3c00514
ACS EST Engg. XXXX, XXX, XXX−XXX

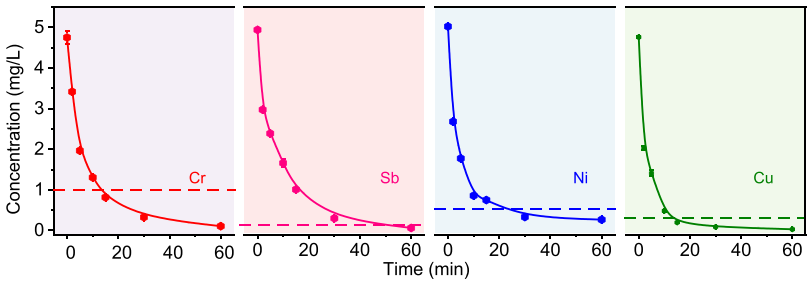

Figure 5. Removal of Cr, Sb, Ni, and Cu from simulated wastewater by FeMg/NC sample. Dashed lines represent the emission regulations of Cr, Sb, Ni, and Cu. (The initial Cr(VI), Sb(V), Ni(II), and Cu(II) concentrations of the simulated wastewater were set to 5 mg/L, followed by the addition of FeMg/NC sample with 1, 2.5, 2, and 1 g/L, respectively).

delocalization effect accelerates electron transfer from the metal core to the surface, easily promoting the reduction and removal of these heavy metals. Notably, the aromatic-carbon layer plays a crucial role in the inward diffusion of pollutants, which is beneficial for subsequent reduction.[19] In conclusion, we believe that the enhanced pollutant removal capacity of the FeMg/NC samples may have been caused by a combination of the phase-fusional structure reduction and the adsorption of the formed metal oxides and aromatic-carbon layer.

■ ENVIRONMENTAL IMPLICATIONS

Benefiting from its unique rapid heating process, the FJH technology has established significant advantages in the development of excellent environmental materials in terms of simplicity and scalability. Our study effectively exploited the Mg activity for bimetallic modification via the FJH technology, revealing the details of the evolution of the reductive structure during the ultrahigh-temperature process. The highly reductive FeMg/NC sample exhibited excellent performance in the removal of typical heavy metals, including Cr(VI), Sb(V), Ni(II), and Cu(II). Considering the removal of Cr(VI) by the FeMg/NC sample as an example, the adsorption and reduction processes involved were elucidated in detail, with a focus on the reduction mechanism, assisted by DFT calculations. Coincidentally, the FeMg/NC sample also exhibited excellent compatibility with the removal of heavy metals from simulated wastewater (Figure 5), demonstrating its feasibility and great potential to treat complex environmental wastewater. Overall, this work offers novel insights into the rational design of bimetallic nanocomposites with tunable structures and desirable functionalities, paving the way for their application in environmental remediation. Notably, the fabrication of environmental materials using FJH technology is highly scalable, and the process is not limited to the synthesis of reductive materials.

■ ASSOCIATED CONTENT

Supporting Information

The Supporting Information is available free of charge at https://pubs.acs.org/doi/10.1021/acsestengg.3c00514.

Additional experimental methods; Parameters of the material synthesis process, including flash current, voltage, and fitting temperature. Material characterization, including SEM images, XPS analysis, N_2 adsorption−desorption isotherms, and pore size distribution. Batch experiments on the removal of different pollutants, such as Cr(VI), Sb(V), Ni(II), and Cu(II). Supplementary electrochemical analyses (Tafel scans and EIS curves), theoretical calculations of Cr(VI) removal, and soluble Fe species released from materials with and without Cr(VI). Removal experiments of Cr, Sb, Ni, and Cu from simulated wastewater by FeMg/NC sample (PDF)

■ AUTHOR INFORMATION

Corresponding Authors

Shicheng Zhang − *Department of Environmental Science and Engineering, Fudan University, Shanghai 200433, China; Shanghai Technical Service Platform for Pollution Control and Resource Utilization of Organic Wastes, Shanghai 200438, China; Shanghai Institute of Pollution Control and Ecological Security, Shanghai 200092, China;* orcid.org/0000-0001-9994-1385; Email: zhangsc@fudan.edu.cn

Xiangdong Zhu − *Department of Environmental Science and Engineering, Fudan University, Shanghai 200433, China;* orcid.org/0000-0002-8536-7690; Email: zxdjewett@fudan.edu.cn

Authors

Chao Jia − *Department of Environmental Science and Engineering, Fudan University, Shanghai 200433, China*

Liming Sun − *Department of Environmental Science and Engineering, Fudan University, Shanghai 200433, China*

Xuan Wu − *Department of Environmental Science and Engineering, Fudan University, Shanghai 200433, China*

Fengbo Yu − *Department of Environmental Science and Engineering, Fudan University, Shanghai 200433, China*

Litao Lin − *Department of Environmental Science and Engineering, Fudan University, Shanghai 200433, China*

Zhelin He − *Department of Environmental Science and Engineering, Fudan University, Shanghai 200433, China*

Jie Gao − *Department of Environmental Science and Engineering, Fudan University, Shanghai 200433, China*

Complete contact information is available at: https://pubs.acs.org/10.1021/acsestengg.3c00514

Author Contributions

C.J.: conceptualization, methodology, investigation, formal analysis, data curation, visualization, and writing - original draft; L.S. and F.Y.: investigation and data curation; X.W. and L.L.: visualization; Z.H. and J.G.: investigation; S.Z.: resources, supervision, and writing - review and editing; X.Z.: conceptualization, methodology, formal analysis, data curation, supervision, funding acquisition, and writing - review and editing.

https://doi.org/10.1021/acsestengg.3c00514
ACS EST Engg. XXXX, XXX, XXX−XXX

Notes

The authors declare no competing financial interest.

■ ACKNOWLEDGMENTS

This work was supported by the National Natural Science Foundation of China (No. 22276040).

■ REFERENCES

(1) Haddeland, I.; Heinke, J.; Biemans, H.; Eisner, S.; Flörke, M.; Hanasaki, N.; Konzmann, M.; Ludwig, F.; Masaki, Y.; Schewe, J.; Stacke, T.; Tessler, Z. D.; Wada, Y.; Wisser, D. Global water resources affected by human interventions and climate change. *Proc. Natl. Acad. Sci. U. S. A.* **2014**, *111* (9), 3251−3256.

(2) Zou, Y.; Wang, X.; Khan, A.; Wang, P.; Liu, Y.; Alsaedi, A.; Hayat, T.; Wang, X. Environmental remediation and application of nanoscale zero-valent iron and its composites for the removal of heavy metal ions: a review. *Environ. Sci. Technol.* **2016**, *50* (14), 7290−7304.

(3) Huang, P.; Ye, Z.; Xie, W.; Chen, Q.; Li, J.; Xu, Z.; Yao, M. Rapid magnetic removal of aqueous heavy metals and their relevant mechanisms using nanoscale zero valent iron (nZVI) particles. *Water Res.* **2013**, *47* (12), 4050−4058.

(4) Lv, H.; Niu, H.; Zhao, X.; Cai, Y.; Wu, F. Carbon zero-valent iron materials possessing high-content fine Fe^0 nanoparticles with enhanced microelectrolysis-Fenton-like catalytic performance for water purification. *Appl. Catal., B* **2021**, *286*, No. 119940.

(5) Long, M.; Donoso, J.; Bhati, M.; Elias, W. C.; Heck, K. N.; Luo, Y. H.; Lai, Y. S.; Gu, H.; Senftle, T. P.; Zhou, C.; Wong, M. S.; Rittmann, B. E. Adsorption and reductive defluorination of perfluorooctanoic acid over palladium nanoparticles. *Environ. Sci. Technol.* **2021**, *55* (21), 14836−14843.

(6) Sun, J.; Yang, J.; Liu, Y.; Guo, M.; Wen, Q.; Sun, W.; Yao, J.; Li, Y.; Jiang, F. Magnetically-mediated regeneration and reuse of core-shell Fe^0@FeIII granules for in-situ hydrogen sulfide control in the river sediments. *Water Res.* **2019**, *157*, 621−629.

(7) Hu, Y.; Peng, X.; Ai, Z.; Jia, F.; Zhang, L. Liquid nitrogen activation of zero-valent iron and its enhanced Cr(VI) removal performance. *Environ. Sci. Technol.* **2019**, *53* (14), 8333−8341.

(8) Marková, Z.; Šišková, K. n. M.; Filip, J.; Čuda, J.; Kolář, M.; Šafářová, K.; Medřík, I.; Zbořil, R. Air stable magnetic bimetallic Fe−Ag nanoparticles for advanced antimicrobial treatment and phosphorus removal. *Environ. Sci. Technol.* **2013**, *47* (10), 5285−5293.

(9) Li, Y.; Mao, X.; Chen, C.; Zhang, L.; Liu, W.; Wang, X.; He, L.; Xu, T. Highly selective reduction of nitrate by zero-valent aluminum (ZVAl) ball-milled materials at circumneutral pH: important role of microgalvanic cells for depassivation of ZVAl and N_2-selectivity. *Environ. Sci. Technol.* **2023**, *57* (11), 4568−4577.

(10) He, F.; Li, Z.; Shi, S.; Xu, W.; Sheng, H.; Gu, Y.; Jiang, Y.; Xi, B. Dechlorination of excess trichloroethene by bimetallic and sulfidated nanoscale zero-valent iron. *Environ. Sci. Technol.* **2018**, *52* (15), 8627−8637.

(11) Xie, J.; Lei, C.; Chen, W.; Huang, B. Conductive-polymer-supported palladium-iron bimetallic nanocatalyst for simultaneous 4-chlorophenol and Cr(VI) removal: enhanced interfacial electron transfer and mechanism. *J. Hazard. Mater.* **2022**, *424*, No. 127748.

(12) Wang, H.; Zhuang, M.; Shan, L.; Wu, J.; Quan, G.; Cui, L.; Zhang, Y.; Yan, J. Bimetallic FeNi nanoparticles immobilized by biomass-derived hierarchically porous carbon for efficient removal of Cr(VI) from aqueous solution. *J. Hazard. Mater.* **2022**, *423*, No. 127098.

(13) Hu, C. Y.; Lo, S. L.; Liou, Y. H.; Hsu, Y. W.; Shih, K.; Lin, C. J. Hexavalent chromium removal from near natural water by copper−iron bimetallic particles. *Water Res.* **2010**, *44* (10), 3101−3108.

(14) Jahnen-Dechent, W.; Ketteler, M. Magnesium basics. *Clin. Kidney J.* **2012**, *5* (Suppl_1), i3−i14.

(15) Siciliano, A.; Curcio, G. M.; Limonti, C. Hexavalent chromium reduction by zero-valent magnesium particles in column systems. *J. Environ. Manage.* **2021**, *293*, No. 112905.

(16) Lee, G.; Park, J.; Harvey, O. R. Reduction of chromium(VI) mediated by zero-valent magnesium under neutral pH conditions. *Water Res.* **2013**, *47* (3), 1136−1146.

(17) Xu, W.; Yang, T.; Liu, S.; Du, L.; Chen, Q.; Li, X.; Dong, J.; Zhang, Z.; Lu, S.; Gong, Y.; Zhou, L.; Liu, Y.; Tan, X. Insights into the synthesis, types and application of iron nanoparticles: the overlooked significance of environmental effects. *Environ. Int.* **2022**, *158*, No. 106980.

(18) Yu, F.; Jia, C.; Wu, X.; Sun, L.; Shi, Z.; Teng, T.; Lin, L.; He, Z.; Gao, J.; Zhang, S.; Wang, L.; Wang, S.; Zhu, X. Rapid self-heating synthesis of Fe-based nanomaterial catalyst for advanced oxidation. *Nat. Commun.* **2023**, *14* (1), 4975.

(19) Sun, L.; Wu, X.; Jiao, Y.; Jia, C.; Teng, T.; Lin, L.; Yu, F.; He, Z.; Gao, J.; Yan, S.; Shi, G.; Ren, Z. J.; Yang, J.; Zhang, S.; Zhu, X. Millisecond self-heating and quenching synthesis of Fe/carbon nanocomposite for superior reductive remediation. *Appl. Catal., B* **2024**, *342*, No. 123361.

(20) Yao, Y.; Huang, Z.; Xie, P.; Lacey, S. D.; Jacob, R. J.; Xie, H.; Chen, F.; Nie, A.; Pu, T.; Rehwoldt, M.; Yu, D.; Zachariah, M. R.; Wang, C.; Shahbazian-Yassar, R.; Li, J.; Hu, L. Carbothermal shock synthesis of high-entropy-alloy nanoparticles. *Science* **2018**, *359* (6383), 1489−1494.

(21) Liao, M.; Wang, X.; Cao, S.; Li, M.; Peng, X.; Zhang, L. Oxalate modification dramatically promoted Cr(VI) removal with zero-valent iron. *ACS EST Water* **2021**, *1* (9), 2109−2118.

(22) Li, C.; Wang, Z.; Liu, M.; Wang, E.; Wang, B.; Xu, L.; Jiang, K.; Fan, S.; Sun, Y.; Li, J.; Liu, K. Ultrafast self-heating synthesis of robust heterogeneous nanocarbides for high current density hydrogen evolution reaction. *Nat. Commun.* **2022**, *13* (1), 3338.

(23) Luong, D. X.; Bets, K. V.; Algozeeb, W. A.; Stanford, M. G.; Kittrell, C.; Chen, W.; Salvatierra, R. V.; Ren, M.; McHugh, E. A.; Advincula, P. A.; Wang, Z.; Bhatt, M.; Guo, H.; Mancevski, V.; Shahsavari, R.; Yakobson, B. I.; Tour, J. M. Gram-scale bottom-up flash graphene synthesis. *Nature* **2020**, *577* (7792), 647−651.

(24) Jia, C.; Pang, M.; Lu, Y.; Liu, Y.; Zhuang, M.; Liu, B.; Lu, J.; Wei, T.; Wang, L.; Bian, T. Graphene environmental footprint greatly reduced when derived from biomass waste via flash Joule heating. *One Earth* **2022**, *5* (12), 1394−1403.

(25) Liu, T.; Rao, P.; Mak, M. S.; Wang, P.; Lo, I. M. Removal of co-present chromate and arsenate by zero-valent iron in groundwater with humic acid and bicarbonate. *Water Res.* **2009**, *43* (9), 2540−2548.

(26) Xu, Z.; Yu, Y.; Xu, X.; Tsang, D. C.; Yao, C.; Fan, J.; Zhao, L.; Qiu, H.; Cao, X. Direct and indirect electron transfer routes of chromium(VI) reduction with different crystalline ferric oxyhydroxides in the presence of pyrogenic carbon. *Environ. Sci. Technol.* **2022**, *56* (3), 1724−1735.

(27) Li, M.; Shang, H.; Li, H.; Hong, Y.; Ling, C.; Wei, K.; Zhou, B.; Mao, C.; Ai, Z.; Zhang, L. Kirkendall effect boosts phosphorylated nZVI for efficient heavy metal wastewater treatment. *Angew. Chem., Int. Ed.* **2021**, *60* (31), 17115−17122.

(28) Fu, F.; Cheng, Z.; Dionysiou, D. D.; Tang, B. Fe/Al bimetallic particles for the fast and highly efficient removal of Cr(VI) over a wide pH range: performance and mechanism. *J. Hazard. Mater.* **2015**, *298*, 261−269.

(29) Qin, N.; Zhang, Y.; Zhou, H.; Geng, Z.; Liu, G.; Zhang, Y.; Zhao, H.; Wang, G. Enhanced removal of trace Cr(VI) from neutral and alkaline aqueous solution by FeCo bimetallic nanoparticles. *J. Colloid Interface Sci.* **2016**, *472*, 8−15.

(30) Guo, Y.; Zhao, Y.; Yang, T.; Gong, B.; Chen, B. Highly efficient nano-Fe/Cu bimetal-loaded mesoporous silica Fe/Cu-MCM-41 for the removal of Cr(VI): kinetics, mechanism and performance. *J. Hazard. Mater.* **2021**, *418*, No. 126344.

(31) Xue, G.; Wang, Q.; Qian, Y.; Gao, P.; Su, Y.; Liu, Z.; Chen, H.; Li, X.; Chen, J. Simultaneous removal of aniline, antimony and chromium by ZVI coupled with H_2O_2: implication for textile wastewater treatment. *J. Hazard. Mater.* **2019**, *368*, 840−848.

https://doi.org/10.1021/acsestengg.3c00514
ACS EST Engg. XXXX, XXX, XXX−XXX

(32) Li, J.; Bao, H.; Xiong, X.; Sun, Y.; Guan, X. Effective Sb(V) immobilization from water by zero-valent iron with weak magnetic field. *Sep. Purif. Technol.* **2015**, *151*, 276−283.
(33) Cao, Y.; Guo, Q.; Liang, M.; Sun, W. Sb(III) and Sb(V) removal from water by a hydroxyl-intercalated, mechanochemically synthesized Mg-Fe-LDH. *Appl. Clay Sci.* **2020**, *196*, No. 105766.
(34) Li, X.; Dou, X.; Li, J. Antimony(V) removal from water by iron-zirconium bimetal oxide: performance and mechanism. *J. Environ. Sci.* **2012**, *24* (7), 1197−1203.
(35) Feng, J.; Lang, G.; Li, T.; Zhang, J.; Li, T.; Jiang, Z. Enhanced removal performance of zero-valent iron towards heavy metal ions by assembling Fe-tannin coating. *J. Environ. Manage.* **2022**, *319*, No. 115619.
(36) Li, Z.; Dong, H.; Zhang, Y.; Li, J.; Li, Y. Enhanced removal of Ni(II) by nanoscale zero valent iron supported on Na-saturated bentonite. *J. Colloid Interface Sci.* **2017**, *497*, 43−49.
(37) Ling, L.; Zhang, W. X. Reactions of nanoscale zero-valent iron with Ni(II): three-dimensional tomography of the "hollow out" effect in a single nanoparticle. *Environ. Sci. Technol. Lett.* **2014**, *1* (3), 209−213.
(38) Guan, X.; Jiang, X.; Qiao, J.; Zhou, G. Decomplexation and subsequent reductive removal of EDTA-chelated cuII by zero-valent iron coupled with a weak magnetic field: performances and mechanisms. *J. Hazard. Mater.* **2015**, *300*, 688−694.
(39) Qu, G.; Zeng, D.; Chu, R.; Wang, T.; Liang, D.; Qiang, H. Magnetic Fe_3O_4 assembled on nZVI supported on activated carbon fiber for Cr(VI) and Cu(II) removal from aqueous solution through a permeable reactive column. *Environ. Sci. Pollut. R.* **2019**, *26* (5), 5176−5188.
(40) Liu, F.; Shan, C.; Zhang, X.; Zhang, Y.; Zhang, W.; Pan, B. Enhanced removal of EDTA-chelated Cu(II) by polymeric anion-exchanger supported nanoscale zero-valent iron. *J. Hazard. Mater.* **2017**, *321*, 290−298.
(41) Zhang, Z.; Zhang, X.; Peng, X.; Li, Z.; Chen, H.; Zhang, X.; Gong, Y.; Tan, C.; Li, H. The simultaneous removal of co-contaminants pyrene and Cu(II) from aqueous solutions by Fe/Mn bimetallic functionalized mesoporous silica. *Environ. Sci. Pollut. R.* **2022**, *29* (47), 71100−71112.
(42) Li, M.; Mu, Y.; Shang, H.; Mao, C.; Cao, S.; Ai, Z.; Zhang, L. Phosphate modification enables high efficiency and electron selectivity of nZVI toward Cr(VI) removal. *Appl. Catal., B* **2020**, *263*, No. 118364.
(43) Gu, Y.; Xie, D.; Wang, Y.; Qin, W.; Zhang, H.; Wang, G.; Zhang, Y.; Zhao, H. Facile fabrication of composition-tunable Fe/Mg bimetal-organic frameworks for exceptional arsenate removal. *Chem. Eng. J.* **2019**, *357*, 579−588.
(44) Guo, Z. Y.; Si, Y.; Xia, W. Q.; Wang, F.; Liu, H.-Q.; Yang, C.; Zhang, W. J.; Li, W.-W. Electron delocalization triggers nonradical Fenton-like catalysis over spinel oxides. *Proc. Natl. Acad. Sci. U. S. A.* **2022**, *119* (31), No. e2201607119.
(45) Huang, Z.; Liang, J. X.; Tang, D.; Chen, Y.; Qu, W.; Hu, X.; Chen, J.; Dong, Y.; Xu, D.; Golberg, D.; Li, J.; Tang, X. Interplay between remote single-atom active sites triggers speedy catalytic oxidation. *Chem.* **2022**, *8* (11), 3008−3017.
(46) Liang, W.; Wang, G.; Peng, C.; Tan, J.; Wan, J.; Sun, P.; Li, Q.; Ji, X.; Zhang, Q.; Wu, Y. Recent advances of carbon-based nano zero valent iron for heavy metals remediation in soil and water: a critical review. *J. Hazard. Mater.* **2022**, *426*, No. 127993.
(47) Jiang, F.; Yao, Y.; Natarajan, B.; Yang, C.; Gao, T.; Xie, H.; Wang, Y.; Xu, L.; Chen, Y.; Gilman, J.; Cui, L.; Hu, L. Ultrahigh-temperature conversion of biomass to highly conductive graphitic carbon. *Carbon* **2019**, *144*, 241−248.

https://doi.org/10.1021/acsestengg.3c00514
ACS EST Engg. XXXX, XXX, XXX−XXX